ACS OMEGA

http://pubs.acs.org/journal/acsodf

Article

Effect of Structural Variation on Spectral, NLO Properties, and Biological Activity of Pyrrole Hydrazones

Poonam Rawat, Ram Niwas Singh,* Anshu Gautam, Mukesh Kumar, Riya Singh, and Poonam Bharati

Cite This: *ACS Omega* 2022, 7, 29571−29586

Read Online

ACCESS | Metrics & More | Article Recommendations | Supporting Information

ABSTRACT: This paper describes spectral, non-linear optical (NLO), and biological activity variation of pyrrole hydrazones as a result of structural variation. In order to study structure−property variation, pyrrole hydrazones (**3A**, **3B**, and **3C**) were synthesized in both solid and solution phases. The grinding solvent-free method becomes rapid, easy, convenient, useful, sustainable, and eco-friendly green synthesis as compared to the classical solution phase reactions. The structure of pyrrole hydrazones has been elucidated by microanalysis and quantum chemical calculations. The intense emission at λ_{em} 521 nm (**3A** and **3B**) and 617 nm (**3C**) in the visible (green and orange) region with Stokes shifts at 195, 160, and 282 nm reveals that the studied compounds work as good photoluminescent materials. All compounds show strong n−π^* and charge transfer (π−π^*) transitions in the UV−vis region with high extinction coefficients. In the studied systems (**3A**, **3B**, and **3C**), the orbital overlap between σ(NH−O) → σ^*(NH−O) is found due to intra-molecular charge transfer. The first hyperpolarizabilities were found to be 48.83×10^{-30} esu for **3B** and 63.89×10^{-30} esu for **3C**, showing variation with structure. Their high values indicate more suitability for NLO application. Incorporation and/or change in position of electron-withdrawing groups increase the β_0 values of **3B** and **3C** compared to **3A**. The β value also increases monotonically as the polarity of the solvents increases. The red shift in N−H and C═O stretching Fourier-transform infrared bonds is due to the formation of dimers. The synthesized **3A**, **3B**, and **3C** show good antimicrobial activity and are predicted to be potential antibacterial and antifungal drugs. The **3B** has more molar refractivity (122.16 esu) than **3A** and **3C** and correlates well with the calculated binding affinity and experimental antimicrobial data.

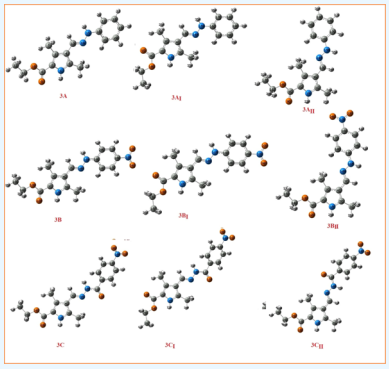

1. INTRODUCTION

Hydrazones possess the −CH═NNH− frame, representing an important class of compounds for drug development and material applications. It contains a C═N double bond and two connected nitrogen atoms of different nature. These structural frames are mainly responsible for variation of physical and chemical properties of hydrazones, thereby attracting researchers to synthesize them as target structures for various applications. Difference in nature of nitrogen atoms provides capability to react with electrophilic and nucleophilic reagents; hence, majority of the hydrazine derivatives are used in the synthesis of heterocyclic compounds and nitrogen-containing organic compounds. Hydrazones display a range of biological spectra.[1−7] The chemical structures of materials and their variety of biological effects are scientifically significant and have been responsible for the development of many technologically relevant fields of interest.

The finding of hidden data and trends is encouraged and facilitated by machine learning (ML). ML allows us to model patterns and correlate data for relationships and predictions. Material properties such as melting point, glass transition temperature, hardness, ionic conductivity, molecular atomization energy, and lattice constant are all used macroscopically and microscopically.[8] To identify a material with better performance from the candidate sets, screening and a probabilistic model are utilized. It is a project that aims to use computational tools to find new materials and assess their properties. To anticipate material attributes, quantitative structure−property relationships (QSPRs) use basic physicochemical features. Density functional theory (DFT) constructs molecular structures using ab initio calculations.[9] In DFT,[10] validation is used to find and forecast interatomic potentials. Validation is used in DFT[10] to search for and forecast interatomic potentials. The various properties are critical for the creation of novel medications, as they determine the pharmacokinetic profile. In chemistry and physics, the DFT approach[11] is used to find the lowest energy state, electronic structure, chemical reactivity, and material properties.[12−16] Chemical information included in a symbolic representation of a molecule is converted into a meaningful number of molecular descriptors that are used to correlate the outcome of a standardized experiment using logic and

Received: February 22, 2022
Accepted: July 20, 2022
Published: August 16, 2022

https://doi.org/10.1021/acsomega.2c00951
ACS Omega 2022, 7, 29571−29586

mathematics. The objective of the present paper is to design and synthesize new organic compounds—pyrrole hydrazones for production of properties. The electro-optical and nonlinear optical (NLO) materials have received considerable attention due to their wide range of potential applications.[16−18] When donor and acceptor groups are present at opposite ends, it leads to significant change and plays an important role in material field, and such materials serve as critical components in several advanced technologies, such as NLO devices, organic light-emitting diodes, photovoltaic cells, and so forth.[17−21]

In light of the preceding literature review, pyrrole hydrazones were produced by reacting formyl pyrrole with aromatic hydrazides containing nitro and carbonyl groups as acceptors and analyzing them using spectroscopic, quantum chemical, and microanalysis. The results show increase in first static hyperpolarizability and activity with incorporated acceptors being responsible for structural variation.

2. EXPERIMENTAL SECTION

The analytical grade chemicals were used as such without further purification. The infrared (IR) spectra were recorded in KBr disc using a Nicolet MX-1 FTIR spectrophotometer. On a Bruker spectrometer, ^{1}H NMR spectra were acquired at 300 MHz (in DMSO-d_6 or methanol solvent), and chemical shifts were reported in parts per million (ppm) units relative to an internal standard, TMS. The UV−vis spectra were recorded using a Shimadzu UV 2100 UV−vis recording spectrophotometer in the 200−800 nm range. UV patterns were recorded in a DMSO solution with a concentration of 10^{-5} M. The mass spectra were recorded using an EI a Micromass Quattro II triple quadrupole mass spectrometer. The melting points were determined using the open capillary tube method, and the data were uncorrected.

2.1. Conventional Method of Synthesis. An ice cold stirring solution of ethyl-4-formyl-3,5-dimetyl-1*H*-pyrrole-2-carboxylate (0.200 g, 1.0251 mmol) (**1**) in methanol was added dropwise to the corresponding hydrazide derivatives (**2A**, **2B**, **2C**) (0.139 g, 1.025 mmol) in 15 mL of methanol with stirring. After stirring at room temperature, the precipitates of cream, orange, and yellow colors were obtained, respectively. The precipitates were filtered off, washed with methanol, and dried in air. Yield: **3A**, 75%, **3B**, 82%, and **3C**, 85%. All compounds decomposed above 250 °C without melting.

2.2. Grinding Method. Equal moles of corresponding hydrazide derivatives with ethyl-4-formyl-3,5-dimetyl-1*H*-pyrrole-2-carboxylate were ground using a mortar and pestle to induce mechanochemical transformations. The reaction progress was checked by TLC. The cream, orange, and yellow colors of **3A**, **3B**, and **3C** solids were recrystallized and dried in air. Yield: **3A**, 97%, **3B**, 99%, and **3C**, 99%

Compound **3A**: (*E*)-ethyl3,5-dimethyl-4-((2-phenylhydrazono)methyl)-1*H*-pyrrole-2-carboxylate: yield: 75%^{S}, 97%^{G}, color: creamy, mp 256 °C (decompose), chemical formula: $C_{16}H_{19}N_3O_2$, elemental analysis: Calcd C, 67.35; H, 6.71; N, 14.73; Obs. C, 67.32; H, 6.69; N, 14.70: ^{1}H NMR DMSO-d_6, 87ft+.

δ (ppm): 1.268−1.315 (t, 3H, J = 6.90, CH_3 ester); 2.366 (s, 3H, pyrrole-CH_3); 2.430 (s, 3H, pyrrole-CH_3); 4.188−4.259 (q, 2H, J = 6.70, CH_2 ester); 6.626−6.74 (d, 1H, Ar-H); 8.758 (d, 1H, J = 8.775, −CH═N−); 138−7.190 (d, 1H, J = 7.80, Ar-H); 6.902−6.928 (s, 1H, Ar-H); 11.403 (s, 1H, hydrazide-NH); 11.503 (s, 1H, pyrrole-NH). ^{13}C NMR (DMSO-d_6, δ (ppm): 158.68 (ester-C═O), 149.93 (hydrazone-CH═N−), 143.519, 122.595, 130.391, 138.608, 139.492 (−CH− phenyl ring), 113.963, 117.531, 115.439, 126.908 (−C− pyrrole ring), 14.595 (α-pyrrole CH_3), 12.087 (β-pyrrole CH_3), 58.351 (ester-CH_2), 10.963 (ester-CH_3). UV−vis absorption spectrum (1×10^{-5} M in DMSO): λ_{max} (nm): 238, 326 nm. DART mass: observed m/z 268.18 [M^+ + 1], calcd 267.14 amu.

Compound **3B**: (*E*)-ethyl 3,5-dimethyl-4-((2-(4-nitrophenyl)hydrazono)methyl)-1*H*-pyrrole-2-carboxylate, yield: 82%^{S}, 99%^{G}, color: orange, mp compound decomposes above 250 °C without melting. Chemical formula: $C_{16}H_{18}N_4O_4$, elemental analysis: Calcd C, 58.17; H, 5.49; N, 16.96; Obs. C, 58.16; H, 5.47; N, 16.95; ^{1}H NMR DMSO-d_6, δ (ppm): 1.281−1.327 (t, 3H, J = 6.90, CH_3 ester); 2.409 (s, 3H, pyrrole-CH_3); 2.438 (s, 3H, pyrrole-CH_3); 4.200−4.271 (q, 2H, J = 6.70, CH_2 ester); 7.793−7.825 (d, 1H, Ar-H); 8.837−8.845 (d, 2H, J = 9.2, Ar-H); 8.750 (s, 1H, CH═N); 11.513 (s, 1H, hydrazide-NH); 11.798 (s, 1H, pyrrole-NH). ^{13}C NMR (DMSO-d_6, δ (ppm): 161.015 (ester-C═O), 135.602 (hydrazone-CH═N−), 149.943, 123.453, 130.315, 143.519, 113.941, 126.908 (−CH− phenyl ring), 115.443, 126.908, 117.641, 128.823 (−C− pyrrole ring), 14.350 (α-pyrrole CH_3), 12.086 (β-pyrrole CH_3), 61.690 (ester-CH_2), 10.963 (ester-CH_3). UV−vis absorption spectrum (1×10^{-5} M in DMSO): λ_{max} (nm): 235, 286 nm, 316 nm. DART mass: observed m/z 330.21 [M^+ + 1], calcd 331.21 amu.

Compound **3C**: (*E*)-ethyl 3,5-dimethyl-4-((2-(4-nitrobenzoyl)hydrazono)methyl)-1*H*-pyrrole-2-carboxylate, yield: 85%^{S}, 99%^{G}, color: yellow, mp decomposes above 280 °C without melting, chemical formula: $C_{17}H_{18}N_4O_5$, elemental analysis: Calcd C, 56.98; H, 5.06; N, 15.63; Obs. C, 56.97; H, 5.04; N, 15.60; ^{1}H NMR DMSO-d_6, δ (ppm):1.27−1.32 (t, 3H, J = 6.90, CH_3 ester); 2.45 (s, 3H, pyrrole-CH_3); 2.40 (s, 3H, pyrrole-CH_3); 4.21−4.28 (q, 2H, J = 6.70, CH_2 ester); 8.37−8.48 (d, 1H, J = 6.90, Ar-H); 8.11−8.13 (d, 1H, J = 6.0, Ar-H); 8.48 (s, 1H, CH═N); 11.67 (s, 1H, hydrazide-NH); 11.76 (s, 1H, pyrrole-NH). ^{13}C NMR (DMSO-d_6, δ (pp): 160.515 (ester-C═O), 139.492 (hydrazone-CH═N−), 148.943, 128.823, 126.908, 135.603, 145.519, 122.595 (−CH− phenyl ring), 115.443, 123.453, 117.641, 130.315 (−C− pyrrole ring), 14.350 (α-pyrrole CH_3), 10.963 (β-pyrrole CH_3), 59.264 (ester-CH_2-), 12.086 (ester-CH_3). UV−vis absorption spectrum (1×10^{-5} M in DMSO): λ_{max} (nm): 265, 335, 468 nm. DART mass observed m/z 359.13 [M^+ + 1], calcd 358.14 amu.

2.3. Antimicrobial Activity. Compounds (**3A**, **3B**, **3C**) and reactants (phenyl hydrazine **2A**, para nitro phenyl hydrazine **2B**, and para nitro benzoic acid hydrazide **2C**) dissolved in DMSO were investigated for their biological activity. As a pharmacological control, DMSO was employed. All chemicals and reactants were tested for bactericidal activity at concentrations of 100 and 200 g/mL. The substance dispersed into the medium's concentration gradient. After the incubation period, the inhibitory zones were measured in centimeters. The actual reading control is represented by the tabulated results. The compounds were tested against *Escherichia coli*, *Pseudomonas aeruginosa* (Gram negative bacteria), *Staphylococcus aureus*, *Streptococcus pyogenes* (Gram positive bacteria), *Candida albicans*, and *Aspergillus niger* (fungi). The plates were placed in an incubator for bacterial growth at 37 °C and for fungal growth at 22 °C within 30 min of preparation. After 48 h of incubation for bacteria and 7 days for fungus, the diameter of the zone (including the diameter

https://doi.org/10.1021/acsomega.2c00951
ACS Omega 2022, 7, 29571−29586

Scheme 1. Formation of Pyrrole Hydrazones (3A, 3B, 3C)

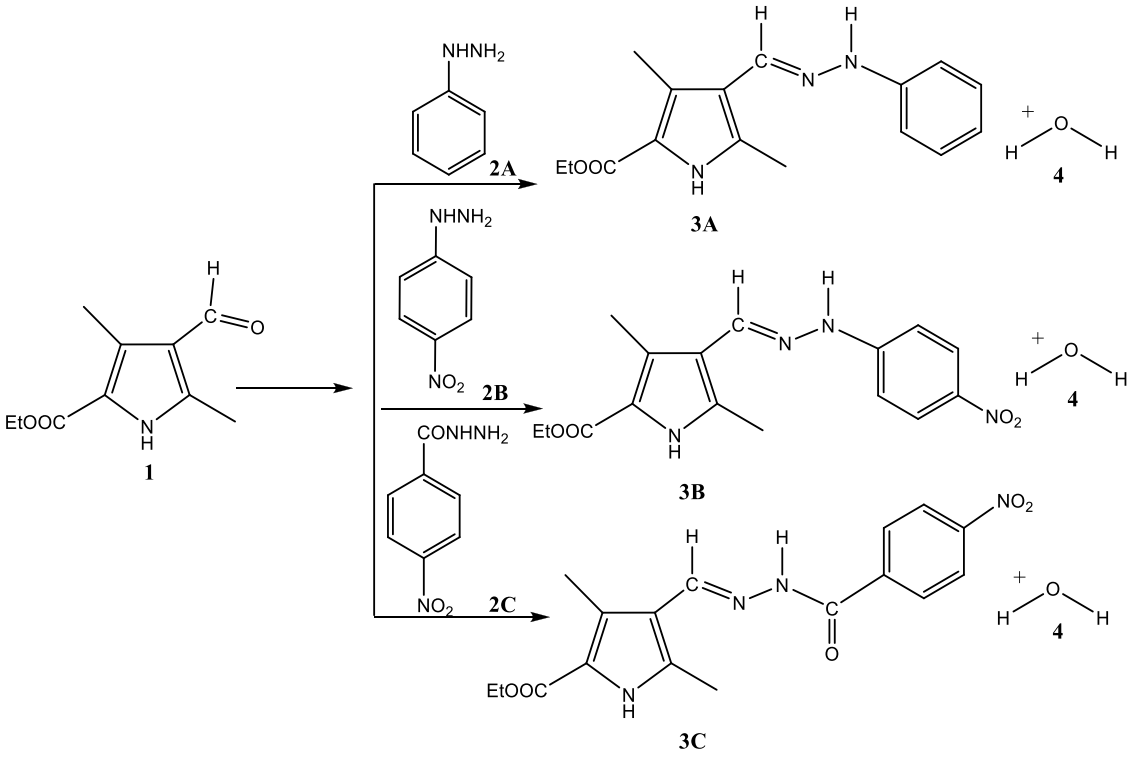

Table 1. Yields and ^{1}H NMR, ^{13}C NMR, MASS, and IR Data of Pyrrole Hydrazones; T = Theoretical Calculated Value, E = Experimental Value, S = Solution Phase, G = Grinding Method

		chemical shifts			
prod.	yield (%)	^{1}H	^{13}C	mass	IR (cm^{-1})
3A	75^{S}, 97^{G}	−N**H** (11.50)^{E}		286.18	NH= (M 3506^{T}) (D 3271^{E}, 3341^{T})
		=NN**H** (11.40)^{E}	**C**OCH$_2$CH$_3$ (158.68)^{E}		−CH=NNH (M 3010^{T}) (3002^{E}, D 3011^{T})
		−C**H**=N− (7.89)^{E}	−**C**H=N (149.94)^{E}		−C=N (M 1599) (1566^{E}, D 1551^{T})
		−C**H**$_2$CH$_3$ (4.18−4.25)^{E}	−**C**H$_2$ (59.35)^{E}		COCH$_2$ (M 1688^{T}) (1663^{E}, D 1655^{T})
3B	82^{S}, 99^{G}	−N**H** (11.51)^{E}		330.21	NH= (M 3500^{T}) (3228^{E}, D 3341^{T})
		=NN**H** (11.79)^{E}	**C**OCH$_2$CH$_3$ (161.01)^{E}		
		−C**H**=N (8.75)^{E}	−**C**H=N (149.94)^{E}		−C=N (M 1594^{T}) (1589^{E}, D 1601^{T})
		−C**H**$_2$CH$_3$ (4.20−4.271)^{E}	−**C**H$_2$ (61.59)^{E}		COCH$_2$ (M 1691^{T}) (1660^{E}, D 1654^{T})
		−CH$_2$C**H**$_3$ (1.28−1.33)^{E}	−**C**H$_3$ (14.35)^{E}		
3C	85^{S}, 99^{G}	−N**H** (11.67)^{E}	−**C**O (160.64)^{E}	359.13	NH= (M 3498^{T}) (3342^{E}, D 3337^{T})
		=NN**H**−CO (11.76)^{E}	**C**OCH$_2$CH$_3$ (160.51)^{E}		
		−C**H**=N (8.48)^{E}	−**C**H=N (148.94)^{E}		−C=N (M 1604^{T}) (1489^{E} D 1507^{T})
		−C**H**$_2$CH$_3$ (4.21−4.28) E	−**C**H$_2$ (59.26)^{E}		COCH$_2$ (M 1691^{T}) (1668^{E}, D 1655^{T})
		−CH$_2$C**H**$_3$ (1.27−1.32)^{E}	−**C**H$_3$ (14.35)^{E}		−NHC=O (1717)

disc) was measured in mm and recorded. The measurements were taken from the bottom of the plate using a ruler without opening the lid.

2.4. Computational Detail. DFT has progressed from a rising star to a key player in computational quantum chemistry during the last few decades. DFT was used to calculate the conformational geometries of the target molecule.[11] For all calculations, the Gaussian 09 program package[22] was utilized. The global and local indices were calculated using Koopman's approach.[23−25] To obtain the aforementioned indexes, we used single-point computations of the anion and cation at the neutral molecule's optimal geometry, ensuring that the external

https://doi.org/10.1021/acsomega.2c00951
ACS Omega 2022, 7, 29571−29586

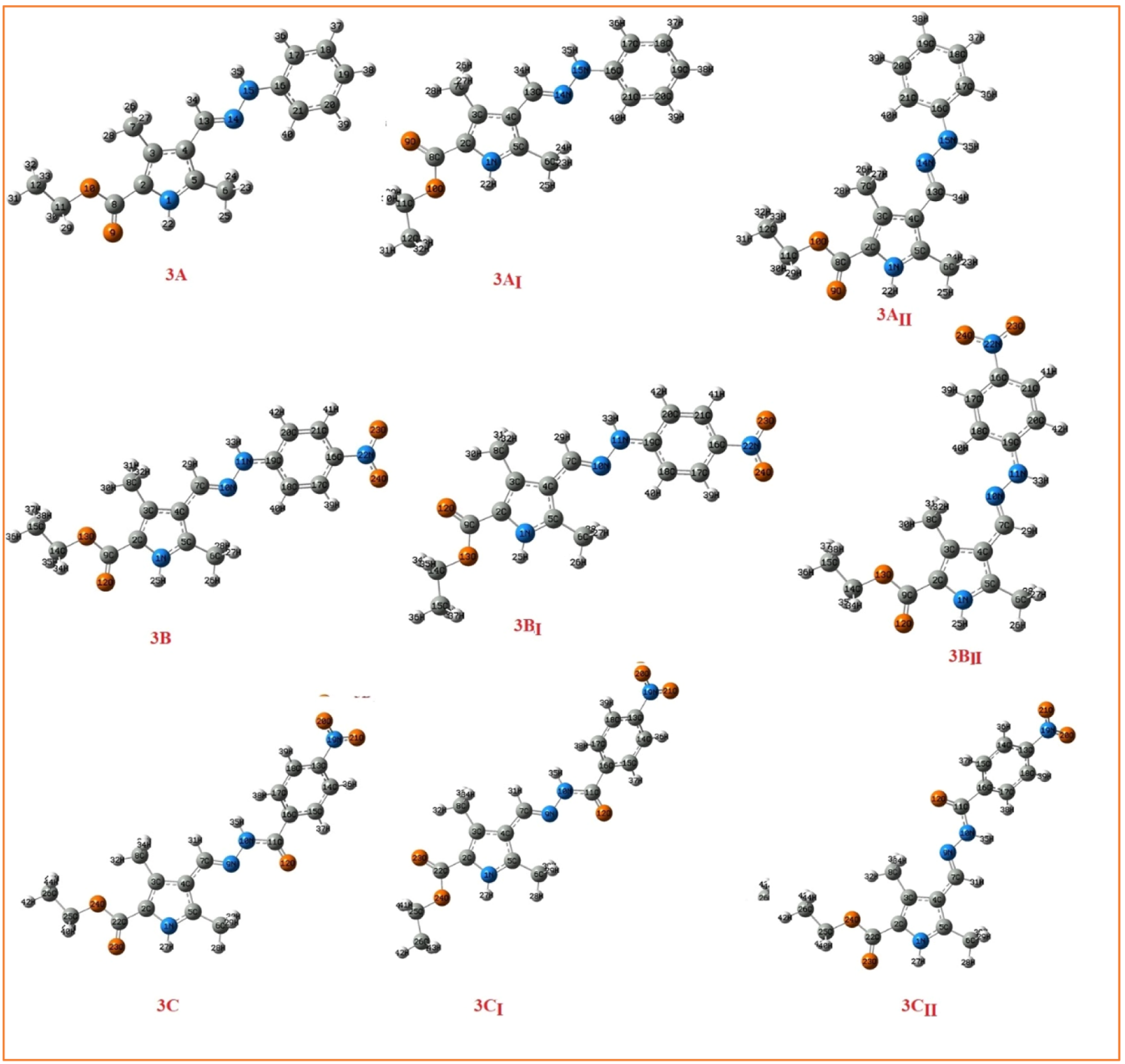

Figure 1. Optimized ground state geometry along with conformers of pyrrole hydrazones (**3A**, **3B**, **3C**).

Table 2. Calculated Enthalpy (au), Gibbs Free Energy (au), and Entropy (Cal (mol Kelvin)$^{-1}$) for 1, 2A/B/C, Products (3A, 3B, 3C), and Water

	1	2A/B/C	product (3A, 3B, 3C)	water	reaction	reaction (kcal/mol)
			Compound A			
enthalpy (H)	−669.1265	−342.7912	−935.5271	−76.3945	−0.0040	−2.5301
Gibbs free energy (G)	−669.1858	−342.8299	−935.6022	−76.4160	−0.0023	−1.4846
entropy (S)	124.946	81.569	157.893	45.116	−3.506	
			Compound B			
enthalpy (H)	−669.1265	−547.2897	−1140.0275	−76.3945	−0.0058	−3.6690
Gibbs free energy (G)	−669.1858	−547.3354	−1140.1084	−76.4160	−0.0031	−1.9628
entropy (S)	124.946	96.122	170.23	45.116	−5.722	
			Compound C			
enthalpy (H)	−669.1265	−660.6235	−1253.3507	−76.3945	0.0047	2.9894
Gibbs free energy (G)	−669.1858	−660.6743	−1253.4367	−76.4160	0.0075	4.7201
entropy (S)	124.946	107.039	181.065	45.116	−5.804	

https://doi.org/10.1021/acsomega.2c00951
ACS Omega 2022, 7, 29571−29586

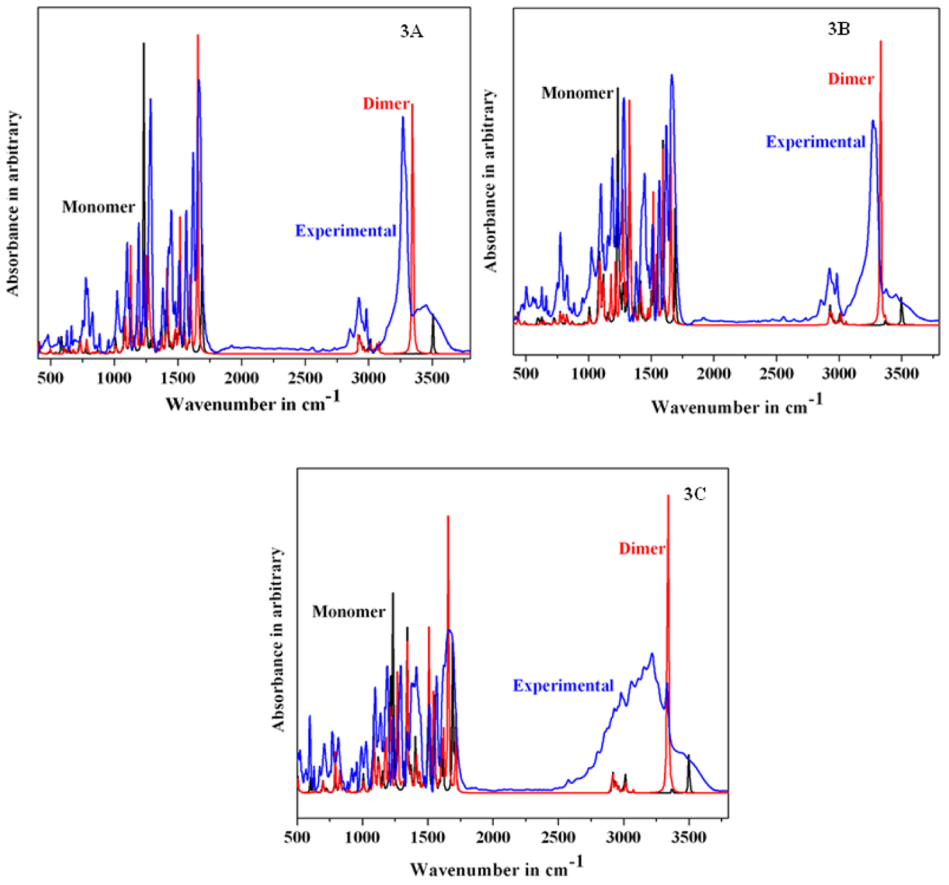

Figure 2. FT-IR simulated spectra of **3A**, **3B**, and **3C**.

potential remained constant. The development of new and more accurate density functionals is a very active research subject. Although efforts are being made to construct more "general-purpose" capabilities, it is understood that some functionalities are better suited to certain applications than others. With a favorable balance of accuracy and computational cost, the B3LYP functional, which uses the basis set 6-311++G(d,p), has been effectively used in reactivity investigations.[11−15] The original geometry constructed from traditional geometrical parameters was reduced at the DFT level without any constraints in the potential energy surface using the standard 6-31G(d,p)/6-311++G(d,p) basis set. The time-dependent DFT was used to determine electronic absorption spectra on the optimized structure (TD-DFT). An online Ramachandran (RC) plot server was used to construct the RC plot.[26] The online Achilles blind docking server application[27] was used to execute the molecular docking investigation. The docking findings were observed using a PYMO visualizer.[28]

3. RESULTS AND DISCUSSION

3.1. Structural Elucidation and Thermodynamics Consideration. Finding novel materials with good performance is a constant issue in materials research. Elements are being replaced and structures are being transformed in current experimental and computational screenings for discovery of novel materials. Compositional search space, structural search space, or both are, on the other hand, frequently restricted. Both screening approaches may necessitate a significant amount of calculation or testing, and they usually result in an "exhaustive search" that consumes a significant amount of time and resources. In light of these facts and the benefits of ML, a completely adaptive method combining ML and computational simulation is offered for the "in silico" evaluation and screening of new materials to provide proposals for new and better materials. The route for formation of (**3A**, **3B**, **3C**) is shown in Scheme 1, and characteristic values for identification are given in Table 1. The classical solvated method requires more hours at reflux temperature in order to obtain good yields.

Next, the grinding method was used for the formation of (**3A**, **3B**, **3C**) compounds. In this method, manual grinding of (**2A**, **2B**, **2C**) with **1** can be carried out by using a mortar and

Table 3. Comparison between Experimental and Calculated Electronic Transitions: *E*/eV, Oscillatory Strength (*f*), (λ_{max} in nm)

si. no.	excitation	*E* (eV)	(*f*)	λ_{cal}	$\lambda_{exp.}$	assignment
			Compound 3A			
1	76 → 77	3.7774	0.6249	328.23	326	$\pi \rightarrow \pi^*$ (CT)
2	76 → 78	3.9717	0.3061	312.17		$\pi \rightarrow \pi^*$
3	75 → 77	5.149	0.2854	240.79	238	$\pi \rightarrow \pi^{**}$
			Compound 3B			
1	87 → 88	3.2315	0.7857	383.68	361	$\pi \rightarrow \pi^*$ (CT)
2	86 → 88	4.0323	0.1438	307.48	286	n → π^*
3	86 → 90	5.2254	0.3828	237.27	235	n → π^*
			Compound 3C			
1	94 → 95	2.6813	0.1248	462.4	468	$\pi \rightarrow \pi^*$ (CT)
2	94 → 96	4.1127	0.6275	301.47	335	$\pi \rightarrow \pi^*$
3	93 → 96	4.7851	0.2469	259.11	265	n → π^*

https://doi.org/10.1021/acsomega.2c00951
ACS Omega 2022, 7, 29571−29586

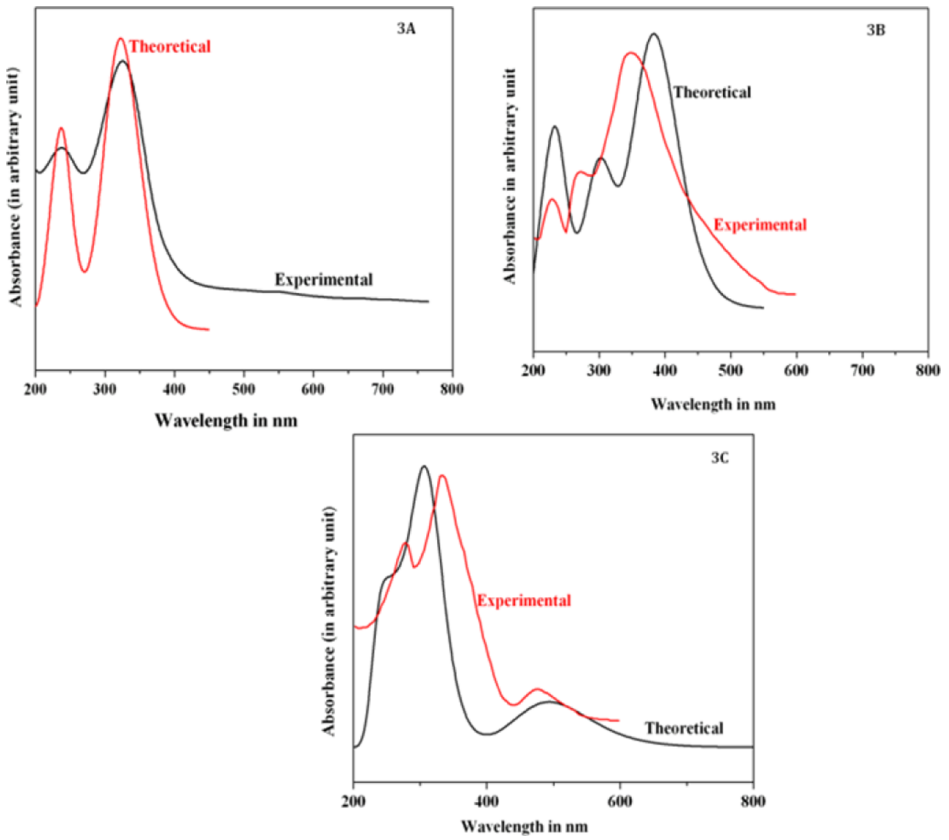

Figure 3. Experimental UV−visible spectra of **3A**, **3B**, and **3C**.

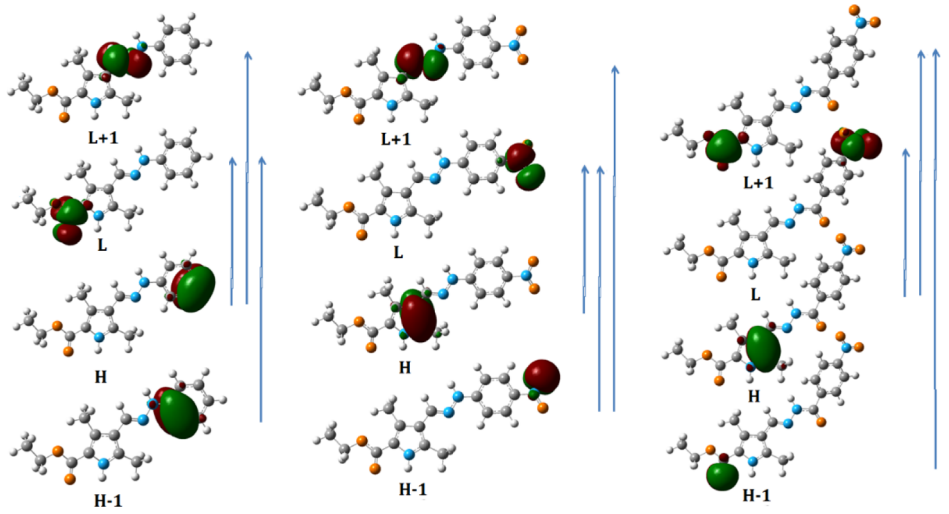

Figure 4. Molecular orbital plots of (**3A**, **3B**, and **3C**) compounds.

pestle. The chemical reaction proceeds due to collisions between the reacting molecules. Pyrrole hydrazones were synthesized in higher yields using this approach. The most frequent method for inducing mechanochemical reactions is grinding using a mortar and pestle.

The geometrical parameters of (**3A**, **3B**, **3C**) have been calculated by DFT/B3LYP levels with the 6-31G**(d,p) basis set and are listed in the Supporting Information Table 1, and the optimized configuration of monomer and conformers is shown in Figure 1. The optimized configuration of dimers along with numbering and labeling is given in the Supporting Information Figure 1. Because these compounds lack crystal structures, the best structures can only be compared to other related systems with optimized configurations. In good percentage yields, new pyrrole hydrazone compounds were produced. The synthesized derivatives are stable, and they can be kept at room temperature for longer periods of time. The structures of synthesized compounds were not only confirmed by IR, ^{1}H and ^{13}C NMR, elemental analysis, UV−vis, and mass spectrometry but also with the electronic descriptors. Further conformational analysis has been performed without imposing any symmetry constraints on the molecule to understand the conformers' stability. The potential energy of **3A**, **3B**, and **3C** was determined by the variation in the total energy of the

https://doi.org/10.1021/acsomega.2c00951
ACS Omega 2022, 7, 29571−29586

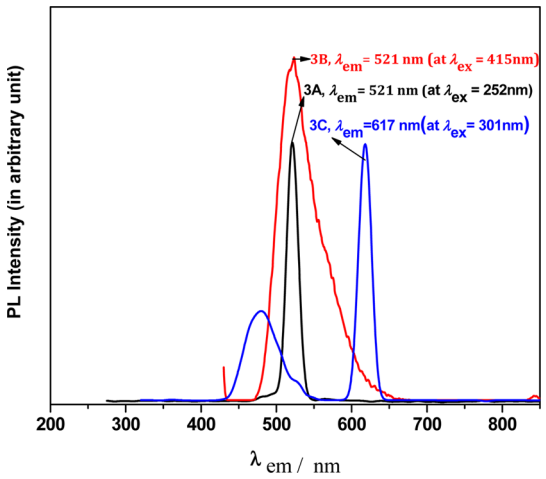

Figure 5. Experimental PL spectra of **3A**, **3B**, and **3C**.

Table 4. Static Dipole Moment ($\mu 0$), Mean Polarizability ($|\alpha 0|$), Anisotropy of Polarizability ($\Delta\alpha$), First Hyperpolarizability ($\beta 0$), and Their Components

	Vacuum			
	dipole moment (μ_0)	polarizability		first hyperpolarizability (β_0)
		α_0	$\Delta\alpha$	
3A	1.66	30.12	118.05	17.71
3B	8.72	35.41	143.54	48.83
3C	6.100	33.80	130.81	63.89
PNA	7.169	5.987	25.871	11.548
	$CHCl_3$			
3A	1.9631	26.089	122.78	27.986
3B	10.088	44.444	181.09	139.772
3C	6.5181	40.431	154.09	117.118
PNA	8.6890	14.6410	53.2540	28.2031
	MeOH			
3A	2.119	27.863	130.47	32.037
3B	10.658	48.223	196.61	195.918
3C	6.889	43.045	162.22	137.598
PNA	9.266	16.107	59.177	38.5141
	DMSO			
3A	2.129	27.971	130.914	32.266
3B	10.691	48.450	197.546	199.669
3C	6.913	43.200	162.68	138.763
PNA	9.300	16.1963	59.5405	39.2014

molecule with change in dihedral angles (C3C2C9O10)/(C5C4C13N14) **3A**, (C3C2C9O13)/(C5C4C7N10) **3B**, and (C3C2C22O24), (C5C4C7N9) in **3C**, as shown in Figure 1. Two minima were observed in the potential energy curve around the dihedral angles (C3C2C9O10)/(C5C4C13N14) **3A**, (C3C2C9O13)/(C5C4C7N10) **3B**, and (C3C2C22O24), (C5C4C7N9) **3C** which correspond to the conformers **3A**/$\mathbf{3A_I}$/$\mathbf{3A_{II}}$, **3B**/$\mathbf{3B_I}$/$\mathbf{3B_{II}}$, and **3C**/$\mathbf{3C_I}$/$\mathbf{3C_{II}}$. The **3A**, **3B**, and **3C** are lower in energy than the latter one and thus represent the more stable conformers. The enthalpy differences between conformers **3A**/$\mathbf{3A_I}$/$\mathbf{3A_{II}}$, **3B**/$\mathbf{3B_I}$/$\mathbf{3B_{II}}$, **3C**/$\mathbf{3C_I}$/$\mathbf{3C_{II}}$ are 0.251, 0.7275, 0.323, 0.773, 0.252, and 1.281 kcal/mol. All calculations have been performed on stable conformers which would correspond to lower energy value that is the conformers **3A**, **3B**, and **3C**. The calculated thermodynamic parameters are listed in Table 2. The calculated negative values show that reactions **3A**, **3B**, and **3C** are spontaneous and exothermic at room temperature.

3.2. Assignments of Vibrational Frequencies Based on Experimental Values and Theoretical Calculations. For the identification of functional groups in organic compounds, vibrational spectroscopy is used extensively.[29] The frequency agreement between estimated harmonics and observed fundamental modes can be used to propose complicated system assignment. The simulated IR spectra are shown in Figure 2, and experimental spectra are given in the Supporting Information Figure 2. The resulting vibrational wave numbers for the optimized geometries of (**3A**, **3B**, **3C**) and the proposed brief assignments are given in Table 1. The detailed vibrational analysis carried out with the help of PED for (**3A**, **3B**, **3C**) is given in the Supporting Information Table 2a−c, respectively.

In the experimental FT-IR spectra of (**3A**, **3B**, **3C**), the N−H stretching vibrations of pyrrole (ν_{N-H}) are observed at 3271, 3269, and 3342 cm^{-1} and calculated as 3341, 3342, and 3337 cm^{-1} in the dimer and 3506, 3507, and 3498 cm^{-1}, respectively, in the monomer. The observed wavenumbers are in good agreement with the calculated wavenumber of dimer than monomer, and similar observation has been found in our earlier studies and also reported in the literature for the hydrogen-bonded dimer of pyrrole.[30−33] As a result, the vibration of the hydrogen-linked N−H group is attributed to the solid-state spectra of (**3A**, **3B**, **3C**). The stretching wavenumber of the hydrogen bond donor (N−H) in the dimer is redshifted due to the elongation of the conventional hydrogen bond donor (N−H bond) compared to the free N−H group in the monomer due to the elongation of the conventional hydrogen bond donor (N−H bond). The computed and observed spectra are found to be very close to each other. Deformation of N−H has appeared at 1517 cm^{-1} and calculated as 1535 cm^{-1}. The solid-state spectrum of (**3A**, **3B**, **3C**) attributes to the vibration of the hydrogen-bonded N−H group, and the observed wagging mode at 774 cm^{-1} also confirms the involvement of pyrrole N−H group in intermolecular attraction. The dimerization tendency enhances in pyrrole species having 3,5-dimethyl substituent along with 2-carbonyl substituent.

3.3. NMR Spectroscopy. The experimental values of ^1H and ^{13}C chemical shifts of (**3A**, **3B**, **3C**) are given in Table 1, and experimental spectra are given in the Supporting Information Figure 2. The comparison between experimental and calculated ^1H and ^{13}C NMR chemical shifts is given in the Supporting Information Table 3a−f. The pyrrolic NH appears as singlets at 9.81, 11.51, and 11.67 ppm in **3A**, **3B**, and **3C**, respectively. The azomethine proton (−CH═N−) and NH proton of the hydrazone (−CH═NNH−) exhibited the expected singlets at 7.89, 8.75, 8.48 and 11.50, 11.79, and 11.74 ppm in DMSO, respectively, in (**3A**, **3B**, **3C**). The higher frequency signal for NH indicates a greater acidity of this hydrogen, which is more susceptible to attack by the solvent. The ethyl ester group attached to the pyrrole ring at α position of (**3A**, **3B**, **3C**) resonated as a quartet (CH_2) in the range of 4.52−4.59 ppm and a triplet (CH_3) at 1.93 ppm.

Given that a comparable molecule's ^{13}C NMR chemical shift range is typically more than 100 ppm, precision ensures that spectroscopic parameters may be reliably interpreted. The synthesis of compounds **3A**−**3C** may be seen in the carbon NMR spectra once more. Supporting Information Table 2 shows ^{13}C NMR spectra. Supporting Information Tables 3b, d,

https://doi.org/10.1021/acsomega.2c00951
ACS Omega 2022, 7, 29571−29586

Table 5. Calculated ε_{HOMO}, ε_{LUMO}, Energy Band Gap ($\varepsilon_L - \varepsilon_H$), Chemical Potential ($\mu$), Electronegativity ($\chi$), Global Hardness ($\eta$), Global Softness ($S$), and Global Electrophilicity Index (ω) for (1), (2), and (3)

molecules	ε_H	ε_L	$\varepsilon_H - \varepsilon_L$	X	μ	H	S	ω	ECT
				Compound **3A**					
(**1**)	−6.1609	−1.0164	5.1446	3.5887	−3.5887	2.5723	0.1944	2.5033	0.52445
(**2a**)	−5.2542	0.36327	5.6176	2.4455	−2.4455	2.8088	0.1780	1.0646	
(**3A**)	−4.8110	−0.6531	4.1579	2.732	−2.7320	2.0790	0.2405	1.7951	
				Compound **3B**					
(**1**)	−6.1609	−1.0164	5.1446	3.5887	−3.5887	2.5723	0.1944	2.5033	−0.4782
(**2b**)	−6.0603	−1.842	4.2183	3.9511	−3.9511	2.1092	0.2371	3.7008	
(**3B**)	−5.4363	−1.959	3.4774	3.7341	−3.7341	1.5123	0.3306	4.6101	
				Compound **3C**					
(**1**)	−6.1609	−1.0164	5.1446	3.5887	−3.5887	2.5723	0.1944	2.5033	−0.8518
(**2C**)	−7.3275	−2.8140	4.5136	5.0707	−5.0707	2.2568	0.2216	5.6967	
(**3C**)	−5.7558	−2.7285	3.0273	4.2422	−4.2422	1.5136	0.3303	5.9445	

Table 6. Selected Reactivity Descriptors as FFs (f_k^+, f_k^-), Local Softnesses (s_k^+, s_k^-), and Local Electrophilicity Indices (ω_k^+, ω_k^-) for (3A, 3B, 3C) Using Hirshfeld Atomic Charges

atom	f_k^+	s_k^+	ω_k^+	atom	f_k^-	s_k^-	ω_k^-
			Compound **3A**				
C8	0.0652	0.0156	0.1170	N1	0.0494	0.0119	0.0888
C13	0.1030	0.0247	0.1850	N15	0.1270	0.0305	0.2281
			Compound **3B**				
C7	0.0926	0.0266	0.3641	N1	0.0493	0.0141	0.1939
C9	0.0236	0.0068	0.0931	N11	0.1129	0.0324	0.4441
			Compound **3C**				
C7	0.0586	0.0193	0.3485	N1	0.0550	0.0181	0.3270
C11	0.0349	0.0115	0.2080	N10	0.0880	0.0290	0.5234
C22	0.0117	0.0038	0.0699				

Table 7. Antimicrobial Activity of Reactants (1, 2A, 2B, 2C) and Products (3A, 3B, 3C) at Different Concentrations

	zone of inhibition(mm)											
	antibacterial activity						antifungal activity					
	Gram positive						Gram negative					
	S. aureus (μg/mL)		*S. pyogenes* (μg/mL)		*E. coli* (μg/mL)		*P. aeruginosa* (μg/mL)		*C. albicans* (μg/mL)		*A. niger* (μg/mL)	
comp	100	200	100	200	100	200	100	200	100	200	100	200
1	4	11	3	5	4	4	4	6	6	7	6	8
2A	5	12	5	8	5	6	5	7	7	8	8	9
2B	7	10	6	9	6	7	5	7	7	8	8	9
2C	7	9	7	8	6	7	6	8	8	9	9	13
3A	10	14	9	14	7	9	9	8	8	14	8	15
3B	11	17	11	17	8	9	10	10	11	16	10	16
3C	12	19	10	18	7	10	9	10	10	17	9	19
control chloramphenicol/nystatin	14	20	13	20	13	23	13	19	12.5	22	14	25

and f show detailed ^{13}C NMR assignments for **3A**, **3B**, and **3C**. The existence of peaks at 158.68, 161.01, and 160.515 ppm in the ^{13}C NMR spectral data of **3A**, **3B**, and **3C** confirms the presence of carbonyl carbon in the ester group. The C═O group connected to the nitro phenyl ring in (**3C**) molecule is confirmed by the peak at 160.64 ppm. In **3A**, **3B**, and **3C**, the C═N−N linked carbon emerges at 149.84, 135.60, and 139.49 ppm, confirming the production of the hydrazone linkage. The estimated ^{1}H and ^{13}C NMR chemical shifts match the observed results very well. In material property prediction research, regression analysis methods are often used, and both macroscopic and microscopic properties can be predicted. The regression correlation between experimental ^{1}H/^{13}C NMR chemical shift (y) and calculated ^{1}H/^{13}C NMR chemical shift (x) (δ in ppm) follows the linear equation, $y = 1.09322x + 0.23132$/$y = 1.09432x + 0.23232$, and the value of correlation coefficient ($R^2 = 0.9298$/0.9529) shows that there is good agreement between experimental and calculated results.

Mass spectrometry has also corroborated more evidence for the production of **3A**, **3B**, and **3C**. Supporting Information Figure 2 shows the mass spectra. The M^+ and M + 1 peak in the mass spectra of the pyrrole hydrazones (**3A**, **3B**, and **3C**) correspond to the molecular weight of the molecules.

3.4. NBO and UV−vis Spectroscopy. From a theoretical standpoint, characterization of excited states can be accomplished by solving the eigenvalue issue using either a multiconfigurational ansatz or the single-particle Kohn−Sham equations in the density functional theory's time-dependent

https://doi.org/10.1021/acsomega.2c00951
ACS Omega 2022, 7, 29571−29586

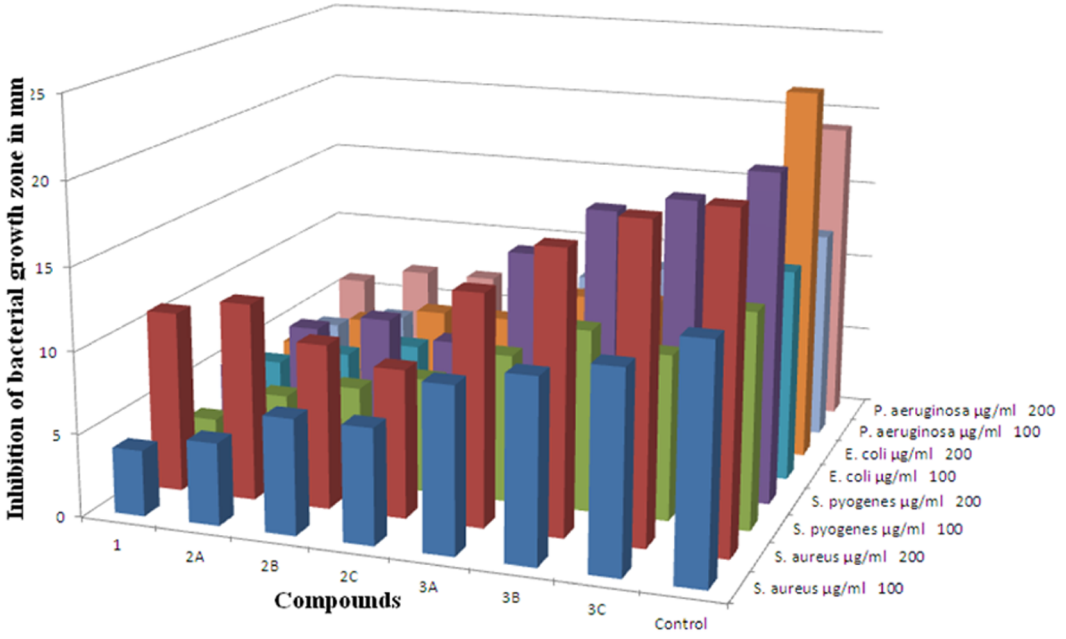

(A)

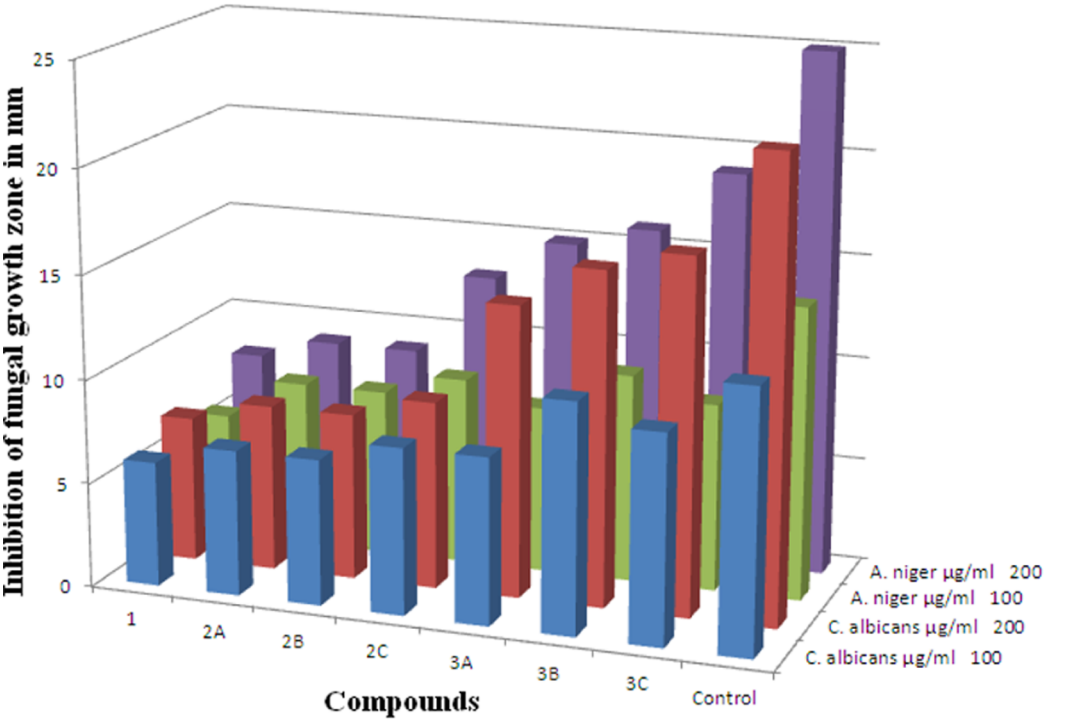

(B)

Figure 6. Bar diagrams representing the inhibition zones against (A) bacterial and (B) fungal strains.

formalism (TDDFT). The transition dipole moment and the accompanying transition density define an excited state. The former informs about the likelihood of exciting an electron from the ground state and the most efficient light polarization

https://doi.org/10.1021/acsomega.2c00951
ACS Omega 2022, 7, 29571−29586

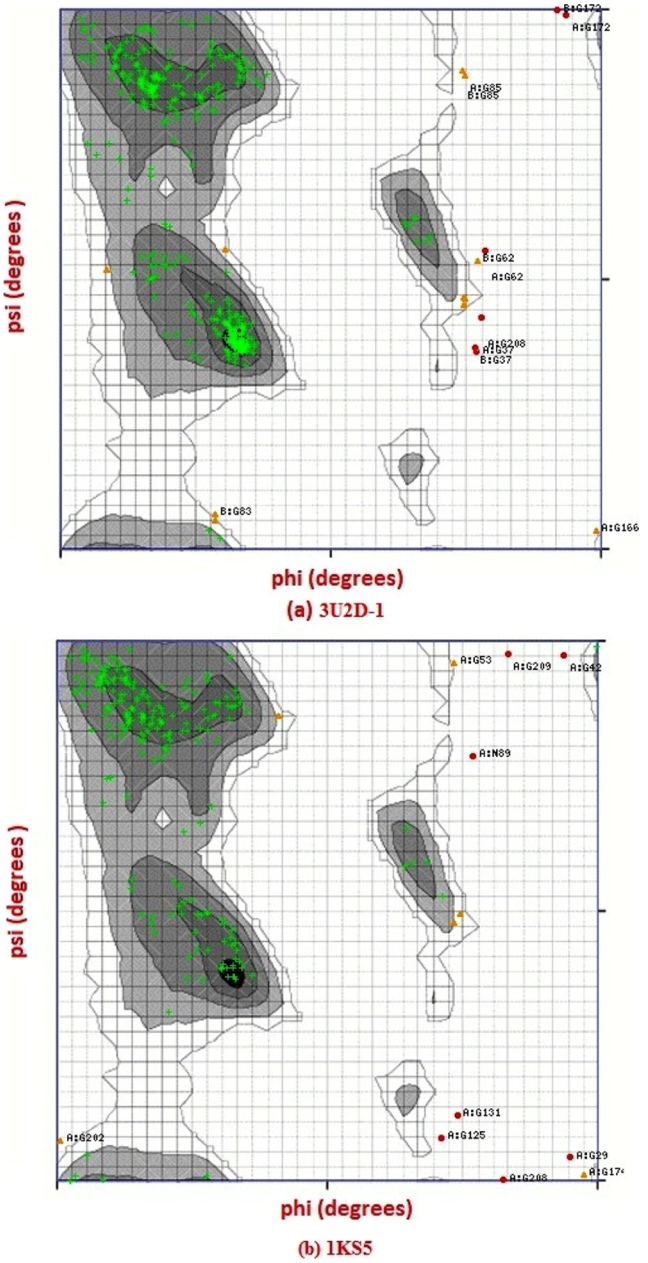

Figure 7. 2D RC plots for receptor proteins (a) 3U2D-1 and (b) 1KS5.

direction, whereas the transition density informs about the shift in electronic density from the ground state to the excited state. Both of these features are particularly sensitive to polarization caused by the environment, and the spectroscopic fingerprint of the isolated molecule in vacuum is frequently insufficient even for a qualitative description. The singlet excited states for the studied compounds are listed in Table 3 and shown in Figure 3. The molecular orbital plots are shown in Figure 4. The UV−visible spectrum analysis reveals that (**3A**, **3B**) are transparent throughout the visible range, with absorption values at 326 and 361 nm, respectively. Molecules with high extinction coefficients allow for strong $\pi-\pi^*$, $n-\pi^*$, and charge transfer transitions in the UV−vis range. In comparison to **3A** and **3B**, compound **3C** has the strongest acceptor and the smallest energy difference between the ground and excited states; thus, absorption occurs in the longer wavelength zone.

The calculated λ_{max} of **3B** has been observed at longer wavelength leading to an increase of molecular hyperpolarizability of **3B** compound in comparison to **3A** and **3C**. The hyperconjugative interaction and electron density transfer from the filled lone pair electron were interpreted using the NBO analysis. Nowadays, theoretical methods are utilized to examine various second-order interactions between the filled orbitals of one sub-system and the unfilled orbitals of another sub-system, as well as to anticipate delocalization or hyperconjugation.[34] Supporting Information Table 4a−c reveals substantial intra- and intermolecular hyperconjugative interactions in the second-order perturbation theory analysis of the Fock Matrix in the NBO basis for (**3A**, **3B**, **3C**). In (**3A**, **3B**, **3C**), the intramolecular interaction is created by the orbital overlap between σ(NH−O) and σ^*(NH−O), resulting in intramolecular charge transfer (ICT) and system stability. The interactions π(C2−C3) → $\pi2^*$(C4−C5), π(C2−C3) → $\pi2^*$(C9−C15), π(C4−C5) → $\pi2^*$(C2−C3), and π(C4−C5) → $\pi2^*$(C2−C3) have high stabilization energy in the range of 15.77−25.80 kcal/mol, according to NBO analysis. The ICT can make the molecule more polarized by moving the π-electron cloud from the donor to acceptor, and the ICT must be accountable for the NLO features of the molecule. As a result, the (**3A**, **3B**, **3C**) may be used in the future for NLO material applications. The selected Lewis (bond or lone pair) NBO orbitals of (**3A**, **3B**, **3C**) with their valence hybrids corresponding to the various bonds and lone pairs (lp) are listed in Supporting Information Table 4a−c.

3.5. Emission (Photoluminescence) Spectroscopy. Photoluminescence (PL) is a process in which a substance absorbs and then re-radiates electromagnetic energy (photons). Photoexcitation initiates luminescence (light emission), which is one of many types (excitation by photons). Figure 5 shows the experimental PL spectra of (**3A**, **3B**, **3C**) in dioxane excited at $\lambda_{ex.max}$ = 252, 415, and 301 nm. The most striking feature is that (**3A**, **3B**) give an intense PL emission at $\lambda_{ex.max}$ = 521 nm in the green region upon irradiation by ultraviolet light ($\lambda_{ex.max}$ = 252 and 415 nm), whereas in (**3C**), a weak emission at $\lambda_{ex.max}$ = 478 nm in the blue region and another intense PL emission at $\lambda_{ex.max}$ = 617 nm in the orange region were observed upon irradiation by visible light ($\lambda_{ex.max}$ = 301 nm). As a result of the intense emission in the visible (green and blue) area with Stokes shifts of 195, 160, and 282 nm, the emission spectrum reveals that the examined compounds are a good photoluminescent material.

3.6. NLO Properties. The use of computational calculations to investigate the broad properties of materials is an alternate method of investigation. Polarizabilities and hyperpolarizabilities define a system's behavior in the presence of an applied electric field.[35] As a result, the molecules under study will have a better NLO response and may be suitable for use as a NLO material. The dipole moment is used to investigate the nonbonded type dipole−dipole interactions between molecules; the bigger the dipole moment, the more powerful the intermolecular interactions. Table 4 shows the calculated dipole moment, polarizability, and first static hyperpolarizability values in gas phase and solvents. The dipole moment of (**3B**) is the greatest of them all. According to the dipole moment vector, the pyrrole side acts as a donor, while the benzene side acts as an acceptor. The attachment of nitro-acceptor increases the dipole moment from **3A** to **3B**. Because

https://doi.org/10.1021/acsomega.2c00951
ACS Omega 2022, 7, 29571−29586

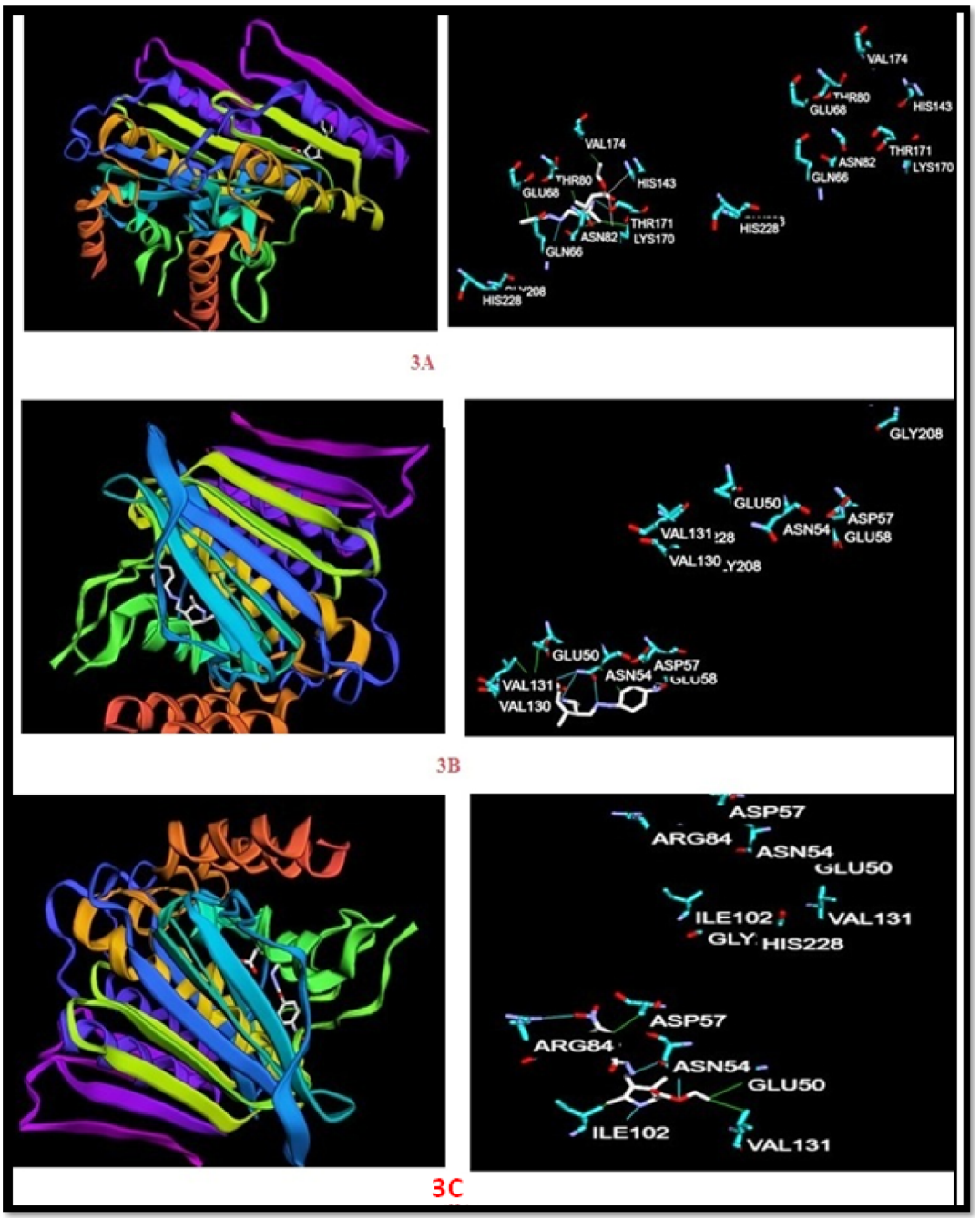

Figure 8. H bond interacting images of the studied compounds (**3A**, **3B**, **3C**) with bacterial receptor protein.

of the carbonyl-acceptor, **3C** has a lower dipole moment than **3B**, in which the vector sum is responsible for the decrease. Due to its maximum softness value, (**3B**) has the highest polarizability value of any. From chloroform to ethanol and DMSO, the dipole moment and polarizability of substances increased monotonically as the solvent polarity of the medium increased. The effects of solvents on NLO characteristics have been explored, and they have been found to change with solvent polarity to varying degrees. In the gas phase, **3C** has the highest first static hyperpolarizability, but **3B** has the highest hyperpolarizability in chloroform, ethanol, and DMSO solvent media. Compounds (**3B**) and (**3C**) have greater first static hyperpolarizability than the commonly used standard p-NA. As a result, the molecules under investigation are anticipated to have a NLO response and could be employed as a NLO material. The UV−visible spectrum analysis reveals that the compounds are nearly transparent in the visible region, with absorption near 300 and 350 nm in the UV range due to the $\pi-\pi^*$ and charge transfer transitions.

3.7. Molecular Electrostatic Potential Map and Electronic Reactivity Descriptor. The reactivity map known as the molecular electrostatic potential (ESP) map reveals where charged point-like reagents are most likely to attack organic molecules electrophilically or nucleophilically. The relative polarity of a molecule is visualized via ESP. It can also be used to explain electronegativity, partial charges, chemical reactivity sites, structure−activity correlations, hydrogen bonding, and other molecular interactions, such as biomolecules and pharmaceuticals. In the Supporting Information Figure 3, the ESP map for the monomer and dimer

https://doi.org/10.1021/acsomega.2c00951
ACS Omega 2022, 7, 29571−29586

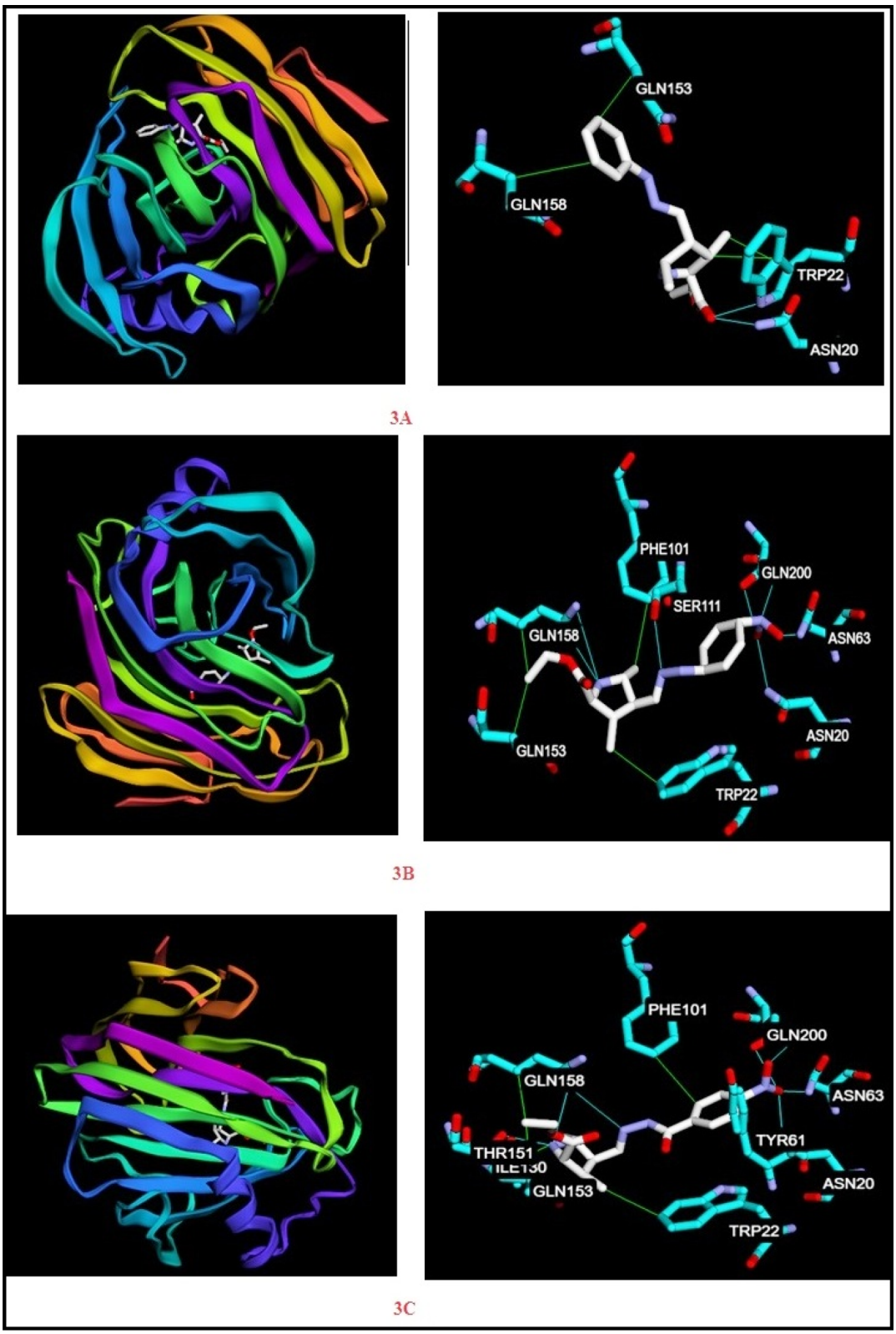

Figure 9. H bond interacting images of the studied compounds (**3A**, **3B**, **3C**) with fungal receptor protein.

of (**3A**, **3B**, **3C**) is displayed. The color code of MEP map is in the range between −0.0511 au (deepest red) and +0.0511 (deepest blue). Negative ESP is frequently associated with the lone pair of electronegative N and O atoms (red or orange blob). ESPs have been equalized, as seen by the decrease in negative potential around the carbonyl group's O oxygen atom and the increase in positive potential around the pyrrole's H hydrogen atom N−H. In the MEP map of monomer, positive potential is only localized over the H hydrogen atom (deep blue blob) of pyrrolic NH, while negative potential is only localized over the O oxygen atom (red blob). The ESP is important in explaining how the examined chemicals (**3A**, **3B**,

https://doi.org/10.1021/acsomega.2c00951
ACS Omega 2022, 7, 29571−29586

3C) interact with biomolecules such as proteins in the living system.

3.8. Global Reactivity Descriptors. To comprehend the link between structure, stability, and global chemical reactivity, conceptual DFT-based global reactivity descriptors are applied. Quantitative structure activity (QSAR), QSPR, and structure toxicity connections are also developed using descriptors. Stability, reactivity, dynamics, and other characteristics are all aided by descriptors. Global reactivity descriptors are essential because they are linked to various electrical structural principles. Electronegativity (χ), chemical potential (μ), global hardness (η), global softness (S), and electrophilicity index (ω) are all global reactivity descriptors that are very good at forecasting global reactivity trends. On the basis of Koopman's theorem,[35,36] global reactivity descriptors are calculated using the energies of frontier molecular orbitals ε_{HOMO} and ε_{LUMO} and given by eqs 1−5.

$$\chi = -1/2(\varepsilon_{LUMO} + \varepsilon_{HOMO}) \quad (1)$$

$$\mu = -\chi = 1/2\ (\varepsilon_{LUMO} + \varepsilon_{HOMO}) \quad (2)$$

$$\eta = 1/2\ (\varepsilon_{LUMO} - \varepsilon_{HOMO}) \quad (3)$$

$$S = 1/2\ \eta \quad (4)$$

$$\omega = \mu^2/2\eta \quad (5)$$

The electrophilicity index (ω) is a global reactivity index similar to chemical hardness and chemical potential, according to Parr et al.[35,36] This is a quantifiable quantity that is both positive and definite. When the system acquires an additional electronic charge (N) from the environment, this new reactivity index evaluates the energy stabilization. Because an electrophile is a chemical species capable of accepting electrons from the environment, its energy must drop when accepting an electronic charge, the direction of charge transfer is fully dictated by the electronic chemical potential of the molecule. As a result, its electronic chemical potential must be lower than that of reactants 1 and 2. Electrophilic charge transfer (ECT)[35] is defined as the difference between the ΔN_{max} values of interacting molecules. If we consider two molecules A and B approach to each other (i) if ECT > 0, charge flow from B to A (ii) if ECT < 0, charge flow from A to B. ECT is calculated using eq 6

$$ECT = (\Delta N_{max)A} - (\Delta N_{max})_B \quad (6)$$

where, $(\Delta N_{max})_A = \mu A/\eta A$ $(\Delta N_{max})_B = \mu_B/\eta_B$.

ECT for the reactant system [(**1**) ↔ (**2A**, **2B**, **2C**)] is listed in Table 5. The global electrophilicity index (ω = 5.994 eV) of (**3C**) shows that it behaves as a strong electrophile. ECT is calculated as 0.524 for reactant molecules (**1**) and (**2A**), which indicates that charge flows from (**2**) to (**1**). Therefore, (**1**) acts as the electron acceptor (electrophile) and (**2**) acts as the electron donor (nucleophile). The low value of chemical potential and high value of electrophilicity index for (**1**) favor its electrophilic behavior. In the same way, the high value of chemical potential and low value of electrophilicity index for (**2A**) favor its nucleophilic behavior.

3.8.1. Local Reactivity Descriptors. One of the most extensively utilized local density functional descriptors to characterize chemical reactivity and site selectivity is the Fukui function (FF).[37] The local (condensed) FFs (f_k^+, f_k^-, f_k^0) are determined using the approach described by Yang and Mortier[38] based on a finite difference method employing eqs 7−9 using the same calculation method B3LYP/6-311G+ +(d,p).

$$f_k^+ = [q(N+1) - q(N)]\text{fornucleophilicattack} \quad (7)$$

$$f_k^- = [q(N) - q(N-1)]\text{forelectrophilicattack} \quad (8)$$

$$f_k^0 = 1/2[q(N+1) - q(N-1)]\text{forradicalattack} \quad (9)$$

where N, $N-1$, and $N+1$ are the total electrons present in neutral, cation, and anion states of molecule, respectively.

In addition, local softnesses (s_k^+, s_k^-, s_k^0)[39] and local electrophilicity indices (ω_k^+, ω_k^-, ω_k^0)[39] describe the reactive atoms present within the molecule. These local reactivity descriptors associated with a site k in a molecule are defined with the help of the corresponding "condensed to atom" variants of FF, using the following eqs 10 and 11.

$$s_k^+ = Sf_k^+,\ s_k^- = Sf_k^-,\ s_k^0 = Sf_k^0 \quad (10)$$

$$\omega_k^+ = \omega f_k^+,\ \omega_k^- = \omega f_k^-,\ \omega_k^0 = \omega f_k^0 \quad (11)$$

where +, −, and 0 signs show nucleophilic, electrophilic, and radical attacks, respectively. Equations 10 and 11 predict that the most electrophilic (nucleophilic) site in a molecule is the one providing the maximum value of s_k^+ (s_k^-), ω_k^+ (ω_k^-), respectively.

The selected local reactivity descriptors for reactants (**2A**, **2B**, **2C**) are given in Table 6. Using Hirshfeld charges, the maximum values of local electrophilic reactivity descriptors (f_k^+, s_k^+, ω_k^+) at aldehyde carbon C6 of reactant (**1**) indicates that this is the most electrophilic site. The nucleophilic reactivity descriptor (f_k^-, s_k^-, ω_k^-) analysis of reactants (**2A**, **2B**, **2C**) shows that N20 is the most nucleophilic site. Therefore, the nucleophilic attack of N20 site of reactants (**2A**, **2B**, **2C**) at the most electrophilic site C6 of reactant (**1**) confirms the formation of product molecules (**3A**, **3B**, **3C**) or Schiff base linkage (C═N) in hydrazone.

The global parameters for (**1**), (**2A**, **2B**, **2C**), (**3A**, **3B**, **3C**) and selected reactivity descriptors as FFs (f_k^+, f_k^-), local softnesses (s_k^+, s_k^-), and local electrophilicity indices (ω_k^+, ω_k^-) for (**3A**, **3B**, **3C**) are given in Table 6. Using Mulliken charges, the maximum values of local electrophilic reactivity descriptors (f_k^+, s_k^+, ω_k^+) at C8, C13, C7, C9, C7, C11, and C22 for (**3A**, **3B**, **3C**) indicate that this site is more prone to nucleophilic attack and favor formation of the larger number of heterocyclic compounds.

3.9. Evaluation of Antimicrobial Activity and Molecular Docking. Table 7 reports the antibacterial and antifungal activities of the reactants and products (**3A**, **3B**, **3C**). Figure 6 shows the bar diagram representation of zone of inhibition, in mm, (a) against bacterial strains (b) and fungal strains. The products (**3A**, **3B**, **3C**) show good antibacterial activity in comparison to pyrrole and hydrazide derivatives (reactants).

The products (**3A**, **3B**, **3C**) were found to be more active against Gram positive *S. aureus* and *S. pyogenes* bacterial strains at 200 μg/mL concentration. The reactant (r1) found in most of the cases is less active against both Gram positive and Gram negative bacteria. The results of preliminary antifungal activity screening reveal that (**3A**, **3B**, **3C**) have a significant effect on *C. albicans* and *A. niger*, even at 100 μg/mL concentration, though the best results come only at 200 μg/mL, respectively. In all cases, the assayed substances showed an activity level

https://doi.org/10.1021/acsomega.2c00951
ACS Omega 2022, 7, 29571−29586

against bacterial and fungal lower than that of chloramphenicol and Nystatin, the reference drug.

3.9.1. Molecular Docking. Molecular docking is a powerful tool for investigating the behavior of small molecules in the binding site of target proteins to elucidate fundamental biochemical processes and confirm bioactivity in any chemical structure.[40] PYMOL is used to visualize protein−ligand interactions.[28] The docking study in this paper used the bacterial PDB ID 3U2D-1 and the fungus PDB ID 1KS5. Both proteins' crystal structures were retrieved from the RSCB protein database.[41,42] The pi and psi angles of the RC plot were used to analyze protein−ligand interaction characteristics with bacterial and fungal proteins.[26] The RC plot in Figure 7 is used to predict the structure and stability of proteins.

The residues in the most favored region, allowed region, and generously allowed region are shown by black dark gray, gray light gray, green, and brown patches on the plot, showing the stability of proteins chosen for docking simulation. The majority of the amino acid residues in both proteins are in the permitted zone. The bonded residues in all three derivatives (**3A**, **3B**, **3C**) lie in the permitted region of the RC plot. These findings indicated that all three **3A**, **3B**, and **3C** derivatives have a high affinity for the target protein, implying antibacterial and -fungal activities. The chosen proteins are well-docked with the three examined ligands, and the atoms of the studied compounds bind with several bacterial protein residues, particularly GLU′68, GLN′66, THR′80, ASN′82, THR′171, HIS′143, VAL′174 (**3A**), VAL′130, VAL′131, GLU′50, GLU′58, ASN′54, ASP′57 (**3B**), and ILE′102, ASN′54, ASP′57, VAL′131, and GLU′50 (**3C**). Protein−ligand interacted images/H bond-interacting images are shown in Figure 8 with bacterial receptor protein and fungal protein interactions with ligands are shown in Figure 9 for **3A**, **3B**, and **3C** compounds.

The atoms of the studied compounds are interacted with different residues of fungal proteins, namely, GLN′153, GLN′158, TRP′22, ASN′20 (**3A**), GLN′153, GLN′158, TRP′22, SER′111, PHE′101, GLN′200, ASN′20, ASN′63 (**3B**), and GLN′200, GLN′158, ASN′20, ASN′63, THY′61, TRP′22, PHE′101, THR′151 (**3C**). The molecular docking study result reveals that the **3A**, **3B**, and **3C** compounds have good interaction properties with the receptor molecules and they are predicted to be potential antibacterial and antifungal drugs.

3.10. Molar Refractivity. Molar refractivity (MR) is a property that is determined by the refractive index, molecular weight, and density of steric bulk and is responsible for the lipophilicity and binding properties of the examined system. It can be calculated by the Lorentz−Lorentz equation[43,44] and defined as

$$\mathrm{MR} = [(n^2 - 1)\,(n^2 + 2)](\mathrm{MW}/\rho) = 1.333\pi N\alpha_0$$

where n—refractive index, MW—molecular weight, ρ—density, (MW/ρ)—molar volume, N—Avogadro number, and α_0—polarizability of molecular system. This equation holds for both liquid and solid states of the system.

The MR property is a crucial one in the QSPR connection. The true volume of the molecule is represented by the MR. MR is affected by the London dispersive forces that work in the drug−receptor interaction, as well as the volume of the molecules. In QSAR investigations for drug design, RM is often used. The calculated MRs for (**3A**, **3B**, and **3C**) are 70.25, 122.16, 108.92 esu, respectively, which are responsible for the binding property of pyrrole hydrazone molecules for treatment of microbial infections. The MR value of **3B** is greater than those of **3A** and **3C**. The maximum bacterial and fungal strains' zone of inhibition was seen in the case of **3B**. The calculated binding affinity correlates well with the experimental antimicrobial result of **3B**.

4. CONCLUSIONS

In this study, pyrrole hydrazones of different structures were synthesized and analyzed using spectral, quantum chemical, and biological methods. Grinding has proven to be a versatile, easy-to-use, highly functional, and environmentally benign method for solid-state synthesis of the **3A**, **3B**, and **3C**. The results revealed that **3A**, **3B**, and **3C** could be obtained with a transformation rate of more than 99%, with no by-products. This is well-suited to the production of active medicinal substances, which necessitates a high level of purity. The computed chemical shifts for ^{1}H and ^{13}C NMR agree with the experimental chemical shifts. The presence of the intermolecular hydrogen bonding N−H···O is confirmed by the red shift in the wavenumber of both the proton donor as pyrrole N−H and the proton acceptor as C═O. The molecular orbital coefficient analysis suggests the nature of all the electronic excitations as $\pi \rightarrow \pi^*$ and n $\rightarrow \pi^*$. The compounds (**3A** and **3B**) show emission at λ_{em} 521 nm, whereas **3C** shows emission at 617 nm in the visible (green and orange) region. The Stokes shifts for **3A**, **3B**, and **3C** are 195, 160, 282 nm, respectively. The NBO analysis indicates that the maximum conjugation stabilization energy is ∼22.68 kcal/mol through $\pi \rightarrow \pi^*$ interactions in the pyrrole ring. The interaction n $\rightarrow \pi^*$ also stabilizes the molecule to a greater extent of 50.68 kcal/mol. The global electrophilicity index for (**3A**, **3B**, **3C**) shows that these molecules behave as strong electrophiles. The electrophilic reactivity descriptor (f_k^+, s_k^+, ω_k^+) analysis for (**3A**, **3B**, **3C**) indicates that the investigated molecules might be used as the precursor for the target synthesis of new heterocyclic derivatives. The compound exhibits strong and effective ICT due to transfer of π-electron cloud from donor to acceptor and shows high hyperpolarizability. The calculated first hyperpolarizabilities (β_0 = 17.71, 48.83, and 63.89 × 10^{-30} esu) demonstrates that the target compounds are attractive materials for NLO applications. The gradual increase in β_0 values of products **3B** and **3C** compared to **3A** is due to the incorporation of electron-withdrawing groups. The products (**3A**, **3B**, and **3C**) display good antimicrobial activity.

■ ASSOCIATED CONTENT

Supporting Information

The Supporting Information is available free of charge at https://pubs.acs.org/doi/10.1021/acsomega.2c00951.

Optimized coordinates and ^{1}HNMR, ^{13}C NMR, UV−vis, and mass spectra (PDF)

Dimer, experimental spectra, and MEP of compounds 3A, 3B, and 3C (PDF)

■ AUTHOR INFORMATION

Corresponding Author

Ram Niwas Singh − *Department of Chemistry, University of Lucknow, Lucknow 226007 Uttar Pradesh, India;* orcid.org/0000-0003-3459-2254; Phone: +91 9451308205; Email: rnsvk.chemistry@gmail.com

https://doi.org/10.1021/acsomega.2c00951
ACS Omega 2022, 7, 29571−29586

Authors

Poonam Rawat − *Department of Chemistry, University of Lucknow, Lucknow 226007 Uttar Pradesh, India*

Anshu Gautam − *Department of Chemistry, University of Lucknow, Lucknow 226007 Uttar Pradesh, India*

Mukesh Kumar − *Department of Chemistry, University of Lucknow, Lucknow 226007 Uttar Pradesh, India*

Riya Singh − *Department of Chemistry, University of Lucknow, Lucknow 226007 Uttar Pradesh, India*

Poonam Bharati − *Department of Chemistry, University of Lucknow, Lucknow 226007 Uttar Pradesh, India*

Complete contact information is available at: https://pubs.acs.org/10.1021/acsomega.2c00951

Notes

The authors declare no competing financial interest.

■ ACKNOWLEDGMENTS

We gratefully acknowledge financial support from the Department of Science and Technology (DST) and NCERT, New Delhi, India. P.R. would like to acknowledge the CSIR, New Delhi, for funding in the form of a Research Associateship (09/107/(0379)/216-EMR-I). The spectroscopic data provided by SAIF, CDRI, Lucknow and IIT, Kanpur are gratefully acknowledged.

■ REFERENCES

(1) Rawat, P.; Singh, R. N. Synthesis, spectral analysis and study of antimicrobial activity of 2,5-diformyl-1H-pyrrole bis(methan-1-yl-1-ylidene)dimalonohydrazone. *J. Chem.* **2019**, *12*, 1219−1233.

(2) Masunari, A.; Tavares, L. C. A new class of nifuroxazide analogues: Synthesis of 5-nitrothiophene derivatives with antimicrobial activity against multidrug-resistant Staphylococcus aureus. *Bioorg. Med. Chem.* **2007**, *15*, 4229−4236.

(3) Oliveira, P. F. M.; Baron, M.; Chamayou, A.; André-Barrès, C.; Guidetti, B.; Baltas, M. Solvent-free mechanochemical route for green synthesis of pharmaceutically attractive phenol-hydrazones. *RSC Adv.* **2014**, *4*, 56736−56742.

(4) Ragavendran, J. V.; Sriram, D.; Patel, S. K.; Reddy, I. V.; Bharathwajan, N.; Stables, J.; Yogeeswari, P. Design and synthesis of anticonvulsants from a combined phthalimide-GABA-anilide and hydrazone pharmacophore. *Eur. J. Med. Chem.* **2007**, *42*, 146−151.

(5) Pisk, J.; Đilović, I.; Hrenar, T.; Cvijanović, D.; Pavlović, G.; Vrdoljak, V. Effective methods for the synthesis of hydrazones, quinazolines, and Schiff bases: reaction monitoring using a chemometric approach. *RSC Adv.* **2020**, *10*, 38566−38577.

(6) Verma, G.; Marella, A.; Shaquiquzzaman, M.; Akhtar, M.; Ali, M. R.; Alam, M. A. A review exploring biological activities of hydrazones. *J. Pharm. BioAllied Sci.* **2014**, *6*, 69−80.

(7) Luque-Ortega, J. R.; Rivas, L. Characterization of the leishmanicidal activity of antimicrobial peptides. *Methods Mol. Biol.* **2010**, *618*, 393−420.

(8) Mahmood, A.; Wang, J. L. Machine learning for high performance organic solar cells: current scenario and future prospects. *Energy Environ. Sci.* **2021**, *14*, 90−105.

(9) Mahmood, A.; Irfan, A.; Wang, J. Machine learning and molecular dynamics simulation-assisted evolutionary design and discovery pipeline to screen efficient small molecule acceptors for PTB7-Th-based organic solar cells with over 15% efficiency. *J. Mater. Chem. A* **2022**, *10*, 4170−4180.

(10) Nagai, R.; Akashi, R.; Sugino, O. Completing density functional theory by machine learning hidden messages from molecules. *Comput. Mat.* **2020**, *6*, 43.

(11) Hohenberg, P.; Kohn, W. Inhomogeneous electron gas. *Phys. Rev.* **1964**, *136*, B864.

(12) Young, D. *Computational Chemistry: A Practical Guide for Applying Techniques to Real Problem*, 3rd ed.; Wiley Publication: Canada, 2001; pp 34−50.

(13) Furche, F.; Rappoport, D. Density Functional Methods for Excited States: Equilibrium Structure and Electronic Spectra. *Computational Photochemistry, Chapter III, Vol. 16 Theoretical and Computational Chemistry*; Elsevier: Amsterdam, 2005; pp 93−128.

(14) van Mourik, T.; Bühl, M.; Gaigeot, M. P. Density functional theory across chemistry, physics and biology. *Philos. Trans. R. Soc., A* **2014**, *372*, 20120488. [and the reverences citation therein]

(15) Walker, J. M. *Biomolecular Simulations*; Springer Link, Humana Press, 2013; pp 3−27.

(16) Niehaus, T. A.; Suhai, S.; Della, S. F.; Lugli, P.; Elstner, M.; Seifert, G.; Frauenheim, T. Tight-binding approach to time-dependent density-functional response theory. *Phys. Rev. B: Condens. Matter Mater. Phys.* **2001**, *63*, 085108.

(17) Achelle, S.; Baudequin, C.; Plé, N. Luminescent materials incorporating pyrazine or quinoxaline moieties. *Dyes Pigm.* **2013**, *98*, 575−600.

(18) Chemla, D. S.; Zyss, J. *Nonlinear Optical Properties of Organic Molecules and Crystals*; Academic Press: New York, 1987; pp 34−100.

(19) Marder, S. R.; Sohn, J. E.; Stucky, G. E. *Materials for Nonlinear Optics: Chemical Perspectives*; *ACS Symposium Series*; American Chemical Society: Washington DC, 1991; pp 2−30

(20) Bosshard, C.; Sutter, K.; Pretre, P.; Hulliger, J.; Florsheimer, M.; Kaatz, P.; Gunter, P. *Organic Nonlinear Optical Materials*; Gordon & Breach: Basel, 1995; pp 256−259

(21) Lu, J.; Zhang, L.; Liu, L.; Liu, G.; Jia, G.; Wu, D.; Xu, G. Study of fluorescence properties of several 4-acyl pyrazolone derivatives and their Zn (II) complexes. *Spectrochim. Acta, Part A* **2008**, *71*, 1036−1041.

(22) Frisch, M. J.; et al. *Gaussian 09, Revision B.01*; Gaussian, Inc.: Wallingford, CT, 2010.

(23) Geerlings, P.; De Proft, F.; Langenaeker, W. Conceptual Density Functional Theory. *Chem. Rev.* **2003**, *103*, 1793−1874.

(24) Contreras, R.; Andrés, J.; Domingo, L. R.; Castillo, R.; Pérez, P. Effect of electron-withdrawing substituents on the electrophilicity of carbonyl carbons. *Tetrahedron* **2005**, *61*, 417−422.

(25) Fukui, K. Formulation of the reaction coordinate. *J. Phys. Chem.* **1970**, *74*, 4161−4163.

(26) https://zlab.umassmed.edu/bu/rama/ accessed date 4 April 2022.

(27) https://bio-hpc.ucam.edu/achilles/dashboard accessed date 4 April 2022.

(28) Schrödinger, L.; DeLano, W. *PyMOL*, 2020. Retrieved from http://www.pymol.org/pymol accessed date 4 April 2022.

(29) Silverstein, R. M.; Webster, F. X. *Spectrometric Identification of Organic Compounds*, 6th ed.; Jon Wiley Sons Inc.: New York, 1963; pp 115−120.

(30) Rawat, R.; Singh, R. N. Evaluation of molecular assembly, spectroscopic interpretation, intra-/inter molecular hydrogen bonding and chemical reactivity of two pyrrole precursors. *J. Mol. Struct.* **2014**, *1075*, 462−470.

(31) Rawat, P.; Singh, R. N. Spectral analysis, structural elucidation and evaluation of chemical reactivity of synthesized ethyl-4-[(2-cyano-acetyl)-hydrazonomethyl]-3,5-dimethyl-1H-pyrrole-2-carboxylate through experimental studies and quantum chemical calculations. *J. Mol. Struct.* **2014**, *1074*, 201−212.

(32) Dubis, T. A.; Grabowski, S. J.; Romanowska, B. D.; Misiaszek, T.; Leszczynski, J. Pyrrole-2-carboxylic Acid and Its Dimers: Molecular Structures and Vibrational Spectrum. *J. Phys. Chem. A* **2002**, *106*, 10613−10621.

(33) Dubis, T. A.; Grabowski, S. J. Infrared spectroscopic and theoretical ab initio studies on conformational isomers of methyl pyrrole-2-carboxylate. *J. Mol. Struct.* **2001**, *562*, 107−117.

(34) Weinhold, F.; Landis, C. R. *Valency and Bonding: A Natural Bond Orbital Donor−Acceptor Perspective*; Cambridge University Press: Cambridge, New York, Melbourne, 2005; pp 215−274.

(35) Parr, R. G.; Szentpály, L.; Liu, S. Electrophilicity Index. *J. Am. Chem. Soc.* **1999**, *121*, 1922−1924.
(36) Parr, R. J.; Yang, W. *Density Functional Theory of Atoms and Molecules*; Oxford University Press: New York, 1989; pp 120−140.
(37) Fukui, K. Role of frontier orbitals in chemical reactions. *Science* **1982**, *218*, 747−754.
(38) Yang, W.; Mortier, W. J. The use of global and local molecular parameters for the analysis of the gas-phase basicity of amines. *J. Am. Chem. Soc.* **1986**, *108*, 5708−5711.
(39) Chakraborty, D.; Chattaraj, P. K. Conceptual density functional theory based electronic structure principles. *Chem. Sci.* **2021**, *12*, 6264−6279.
(40) Maria Julie, M.; Prabhu, T.; Elamuruguporchelvi, E.; Asif, F. B..; Muthu, S.; Irfan, A. Structural (monomer and dimer), wavefunctional, NCI analysis in aqueous phase, electronic and excited state properties in different solvent atmosphere of 3-{(E)-[(3,4-dichlorophenyl)-imino]methyl} benzene-1,2-diol. *J. Mol. Liq.* **2021**, *336*, 116335−119345.
(41) https://www.rcsb.org/structure/3u2d accessed date 4 April 2022.
(42) https://www.rcsb.org/structure/1ks5 accessed date 4 April 2022.
(43) Rawat, P.; Singh, R. N. Experimental and DFT study on a newly synthesized ethyl 2-cyano-3-[5-(phenyl-hydrazonomethyl)-1H-pyrrol-2-yl]-acrylate. *J. Mol. Struct.* **2015**, *1081*, 293−303.
(44) Padrón, J. A.; Carasco, R.; Pellón, R. F. Molecular descriptor based on a molar refractivity using Randic-type graph-theoretical invariant. *J. Pharm. Pharm. Sci.* **2002**, *5*, 258.

https://doi.org/10.1021/acsomega.2c00951
ACS Omega 2022, 7, 29571−29586